

## Genetic labeling of axo-axonic cells in the basolateral amygdala

Miki Nakashima<sup>a</sup>, Yuji Ikegaya<sup>a,b,c,\*</sup>, Shota Morikawa<sup>a,b,\*</sup>

<sup>a</sup> Graduate School of Pharmaceutical Sciences, The University of Tokyo, Tokyo 113-0033, Japan

<sup>b</sup> Institute for AI and Beyond, The University of Tokyo, Tokyo 113-0033, Japan

<sup>c</sup> Center for Information and Neural Networks, National Institute of Information and Communications Technology, Suita City, Osaka 565-0871, Japan

### ARTICLE INFO

#### Keywords:

Axo-axonic cell  
BLA  
Vipr2  
Interneuron  
Parvalbumin

### ABSTRACT

GABAergic neurons are classified into multiple subtypes based on morphology, physiological properties, and gene expression profiles. Although traditionally defined axo-axonic cells (AACs) are a unique type of interneuron that expresses *parvalbumin* and innervates the axon initial segment (AIS) of pyramidal neurons, a genetic marker for AACs in the basolateral amygdala (BLA) has not been identified. Here, we show that *vasoactive intestinal peptide receptor 2* (*Vipr2*)-expressing interneurons exhibit anatomical and electrophysiological properties of AACs in the BLA. Using a reporter mouse expressing fluorescent proteins specifically in *Vipr2*<sup>+</sup> cells, we analyzed the distribution, postsynaptic targeting and electrophysiological properties of *Vipr2*<sup>+</sup> cells in the BLA. More than half of the *Vipr2*<sup>+</sup> cells showed parvalbumin immunoreactivity and innervated the AIS of pyramidal neurons in the BLA of *Vipr2*-tdTomato mice. Notably, most of the *Vipr2*<sup>+</sup> cells showed fast-spiking properties. Furthermore, the use of a Cre-dependent adeno-associated virus led to more selective labeling of AACs in the BLA. These results suggest that AACs are genetically identifiable in the BLA without anatomical or physiological analysis.

### 1. Introduction

Axo-axonic cells (AACs) are GABAergic neurons that predominantly form synapses onto the axon initial segment (AIS) of pyramidal neurons (Somogyi, 1977). Light and electron microscopy studies have revealed that traditionally defined AACs are parvalbumin-positive (PV<sup>+</sup>) interneurons, and their axon terminals indicate symmetric synapses in the mouse dentate gyrus and monkey layer 2 of area 4 (Buhl et al., 1994; DeFelipe et al., 1989). Based on morphological characteristics, AACs are also called chandelier cells and are mainly localized in the cortical areas and in the hippocampus (Peters et al., 1982; Somogyi et al., 1985). In the hippocampus, AACs preferentially fire around the peak of theta cycles and become silent at the onset of sharp-wave ripples to consolidate memory formation (Klausberger et al., 2003; Ego-Stengel and Wilson, 2010; Girardeau et al., 2009). In recent studies, cell-type-specific genetic access to AACs in mice has been achieved and revealed that the population activity of AACs in the visual cortex correlated with pupil dilation, a proxy for arousal (Schneider-Mizell et al., 2021), and that AACs in the hippocampal CA1 area are synchronously activated by locomotion or whisking during rest but not sensory stimuli (Dudok et al., 2021). Although the function and the anatomical and physiological features of

AACs have been elucidated in the cortical area and hippocampus, the distribution and function of AACs in other brain regions have not been fully examined.

The basolateral amygdala (BLA), a region critical for emotional memory processing, shows a cortical-like structure (LeDoux, 2000; Sah et al., 2003). Consistent with early studies in the visual cortex and hippocampus, AACs were also observed in the BLA (Bienvenu et al., 2012; Veres et al., 2014). A study using in vivo electrophysiological recording combined with the anatomical identification of cell types revealed that AACs in the BLA increase neuronal activity in response to noxious stimuli such as pinch and foot shock (Bienvenu et al., 2012).

Although AACs are an essential target for anatomical and functional analyses, there are technical difficulties in physiological research that require anatomical post hoc investigation, such as confirmation of axon terminals on the AIS and parvalbumin immunostaining (Bienvenu et al., 2012; Perumal et al., 2021; Veres et al., 2014). A breakthrough advance in the characterization of neuronal subtypes by genetic transcriptome analysis enabled the efficient identification of AACs, and this advance has led to the discovery of novel biochemical markers of interneurons. The first marker of AACs or chandelier cells was parvalbumin (Buhl et al., 1994; DeFelipe et al., 1989). However, this marker is not specific

\* Correspondence to: Laboratory of Chemical Pharmacology Graduate School of Pharmaceutical Sciences, The University of Tokyo 7-3-1 Hongo, Bunkyo-ku, Tokyo 113-0033, Japan.

E-mail addresses: [yuji@ikegaya.jp](mailto:yuji@ikegaya.jp) (Y. Ikegaya), [morikawa-s@mol.f.u-tokyo.ac.jp](mailto:morikawa-s@mol.f.u-tokyo.ac.jp) (S. Morikawa).

<https://doi.org/10.1016/j.neures.2022.02.002>

Received 15 December 2021; Received in revised form 10 February 2022; Accepted 16 February 2022

Available online 18 February 2022

0168-0102/© 2022 Elsevier B.V. and Japan Neuroscience Society. All rights reserved.

for AACs, and most PV<sup>+</sup> interneurons exhibit a basket-like morphology and form synapses with the cell body or dendrite of a neuron (Kawaguchi and Kubota, 1998). Tasic et al. classified the interneuron subtype using single-cell RNA sequencing in the mouse primary visual cortex and anterior lateral motor cortex and proposed *vasoactive intestinal peptide receptor 2* (*Vipr2*) as a new genetic marker of chandelier cells in the mouse neocortex (Tasic et al., 2018). Although some *Vipr2*<sup>+</sup> cells exhibit PV immunoreactivity and classic chandelier-like morphology, with synaptic boutons that are densely arranged in the vertical direction (Tasic et al., 2018), it remains unclear whether *Vipr2* is also a genetic marker of chandelier cells or AACs in subcortical regions, including the BLA. Furthermore, it is necessary to investigate whether *Vipr2*-IRES2-Cre mice can be used to specifically label AACs in the adult BLA.

## 2. Materials and methods

### 2.1. Animals

*Vipr2*-IRES2-Cre knock-in mice (B6. Cg-*Vipr2em1.1*(cre)Hze/J; aged 5–9 weeks; JAX#031332; The Jackson Laboratory, Bar Harbor, ME, USA) and *Ai14* mice (B6;129S6-Gt(ROSA)26Sortm14(CAG-tdTomato)Hze/J; JAX#007908; aged 5–9 weeks; The Jackson Laboratory) were used in this study. Animal experiments were performed with the approval of the Animal Experiment Ethics Committee at The University of Tokyo (approval number: P29–15) and according to the University of Tokyo Guidelines for the Care and Use of Laboratory Animals. These experimental protocols were carried out in accordance with the Fundamental Guidelines for Proper Conduct of Animal Experiments and Related Activities in Academic Research Institutions (Ministry of Education, Culture, Sports, Science and Technology, Notice No. 71 of 2006), the Standards for Breeding and Housing of and Pain Alleviation for Experimental Animals (Ministry of the Environment, Notice No. 88 of 2006) and the Guidelines on the Method of Animal Disposal (Prime Minister's Office, Notice No. 40 of 1995). All animals were housed under a 12-h dark-light cycle (light from 07:00–19:00) at 22 ± 1 °C with ad libitum access to food and water.

### 2.2. Virus production

Recombinant adeno-associated viruses (AAVs) were generated by triple transfection of the 293 AAV cell line (AAV-100; Cell Biolabs, Inc., San Diego, CA) with AAVdj rep-cap, pHelper from the AAV-DJ Helper Free Packaging System (VPK-400-DJ; Cell Biolabs, Inc.) and pAAV-FLEX-GFP (Addgene #28304) or pAAV-EF1α-FLEX-Synaptophysin-mCherry (Liu et al., 2021) using PEI-Max (24765; Polysciences, Inc., Warrington, PA). AAV vectors were purified using the AAVpro Purification Kit All Serotypes (6666; Takara Bio Inc., Shiga, Japan). Virus titers were determined by qPCR using the AAV2 ITR primer pair (Aurnhammer et al., 2012), Luna Universal qPCR Master Mix (M3003S; New England Biolabs, Ipswich, MA, USA) or THUNDERBIRD Next SYBR qPCR Mix (QPX-201; TOYOBO, Osaka, Japan), and the LightCycler qPCR 2.0 system (DX400; Roche, Basel, Switzerland).

### 2.3. Surgical procedures

Mice were anesthetized with isoflurane (Pfizer Inc., New York, NY) and placed in a stereotaxic frame. AAVdj-CBA (chicken β-actin promoter)-FLEX-GFP (3.36 × 10<sup>13</sup> GC/ml, 300 nl) or AAVdj-EF1-FLEX-synaptophysin-mCherry (3.44 × 10<sup>13</sup> GC/ml, 300 nl) was pressure-injected into the basolateral amygdala (BLA; caudal −1.4 mm, lateral 3.4 mm, and ventral 4.1–4.3 mm). All viruses were injected at a rate of 100 nl/min using a syringe pump (KD Scientific Inc., Holliston, MA, USA) connected to glass pipettes (30–0034, Harvard Apparatus, Holliston, MA, USA; and 1B100F-3, World Precision Instruments, Sarasota, FL, USA) with a joint tube (JT10; Eicom, Kyoto, Japan). The

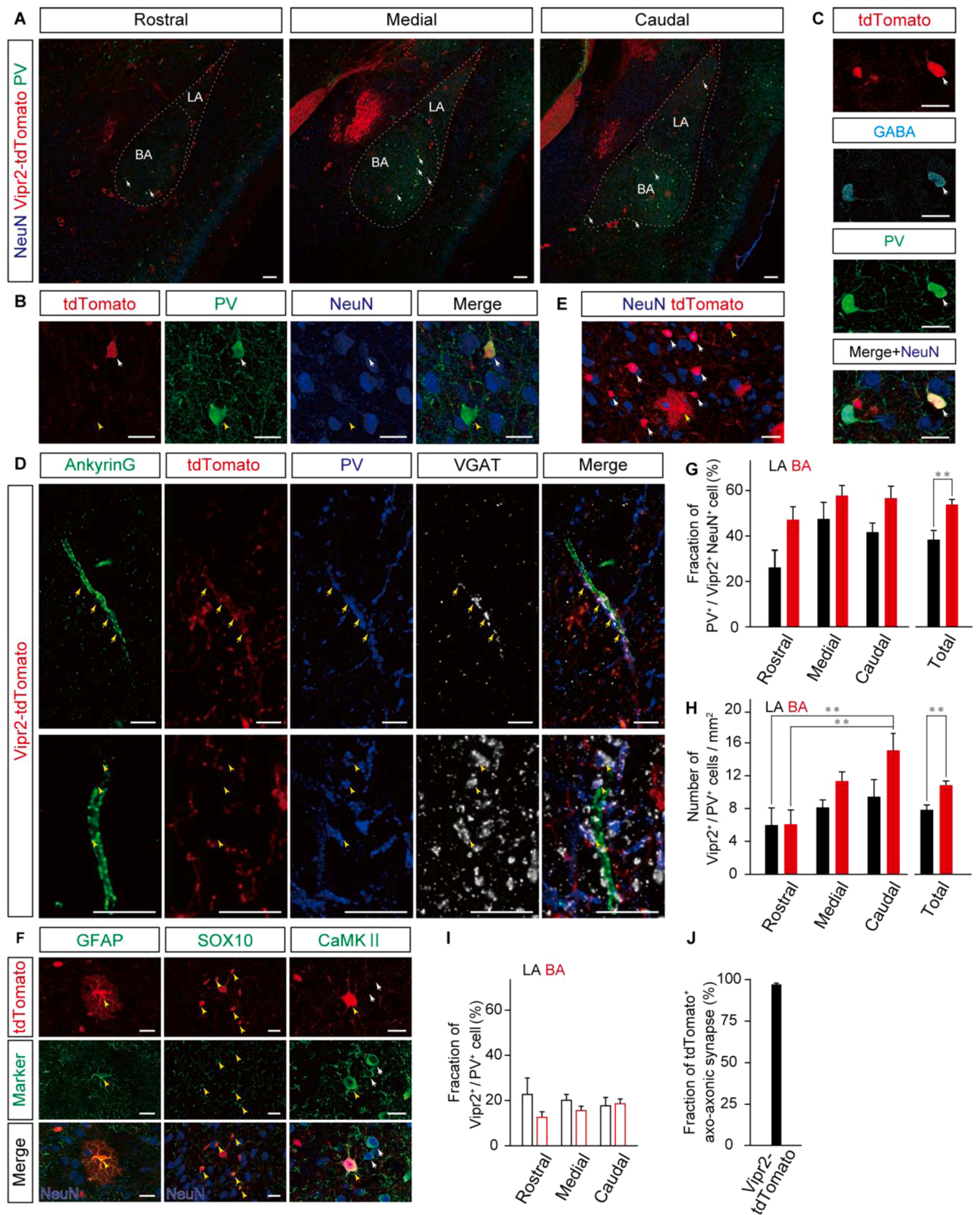
coordination of injection sites was measured from bregma, and ventral measurements were in reference to the surface of the brain. Fourteen to 23 days after virus injection, the mice were transcardially perfused with 0.1 M phosphate-buffered saline (PBS; pH 7.4) followed by 4% paraformaldehyde (PFA; Fujifilm Wako Pure Chemical Corporation, Osaka, Japan) in 0.1 M phosphate buffer (PB; pH 7.4).

### 2.4. Tissue processing

Brains were postfixed overnight at 4 °C in 4% PFA/PB, transferred to 30% (w/v) sucrose in PBS for 48 h, and then cut into 50-μm coronal sections using a cryostat (HM520; Thermo Fisher Scientific Inc., Waltham, MA, USA). The free-floating sections were blocked with 5% bovine serum albumin (BSA, 01863-77; NACALAI TESQUE, INC., Kyoto, Japan) and 0.3% Triton X-100 in PBS for 1 h at room temperature and then incubated overnight at 4 °C with the following primary antibodies: rabbit polyclonal anti-parvalbumin (1:2000; PV-Rb-Af750, Frontier Institute Co., Ltd. Hokkaido, Japan), mouse monoclonal anti-parvalbumin (1:1000; P3088, clone PARV-19, Sigma–Aldrich), guinea pig polyclonal anti-parvalbumin (1:1000; 195 004, Synaptic Systems, Goettingen, Germany), mouse monoclonal anti-NeuN (1:2000; MAB377 clone A60, Merck Millipore, Burlington, MA, USA), guinea pig anti-NeuN (1:1000; 266-004, Synaptic Systems), rabbit polyclonal anti-GABA (1:2000; A2052, Sigma–Aldrich), mouse monoclonal anti-CaMKIIα (1:500, 05-532, clone 6G9, Merck Millipore), rabbit polyclonal anti-ankyrin-G (1:400; AnKG-Rb-Af610, Frontier Institute Co., Ltd.), rabbit polyclonal anti-GFAP (1:1000; G9269, Sigma–Aldrich), guinea pig polyclonal anti-VGAT (1:200; 131 004, Synaptic Systems), and mouse monoclonal anti-SOX10 (1:200; 84720, clone BSB-62, BioLegend, Tokyo, Japan). The following secondary antibodies used in this study were purchased from Thermo Fisher Scientific: Alexa Fluor Plus 405-conjugated donkey anti-mouse IgG (1:1000, A-48257), Alexa Fluor 488-conjugated goat anti-mouse IgG (1:1000; A-11029), Alexa Fluor 488-conjugated goat anti-rabbit IgG (1:1000; A-11034), Alexa Fluor 647-conjugated goat anti-rabbit IgG (1:1000, A-21245), and Alexa Fluor 647-conjugated goat anti-guinea pig IgG (1:1000, A-21450). The DyLight 405-conjugated donkey anti-guinea pig IgG (1:1000, 706–475–148) was purchased from Jackson Immuno Research Laboratories, Inc. (West Grove, PA, USA). Labeled sections were costained with NeuroTrace 435/455 Blue Fluorescent Nissl Stain (1:500; N21479, Thermo Fisher Scientific Inc.) or DAPI (1:2000; D9542–10MG, Sigma–Aldrich, St. Louis, MO, USA) in 0.1 M PBS for 10–20 min at RT and mounted onto microscope slides with Prolong Diamond Antifade Reagent (P36965; Thermo Fisher Scientific). Anatomical borders of brain regions were identified by NeuroTrace or NeuN immunoreactivity referring to the brain atlas (Franklin and Paxinos, *The Mouse Brain in Stereotaxic Coordinates Third Edition*, 2008) and Price, 1987. The sections were scanned using a laser scanning confocal microscope (A1-HD25; Nikon, Tokyo, Japan) equipped with a 10× air objective (CFI Plan Apo Lamda S 10×; NA0.45, Nikon), 20× air objective (CFI Plan Apo VC 20×; NA0.75, Nikon), 40× air objective, and 100× oil objective lens (Apo TIRF 100× Oil, NA1.49, Nikon). The *Vipr2*-tdTomato<sup>+</sup> neurons in the BLA were counted bilaterally using 14–39 (average 24.71 ± 2.86) slices from each mouse. The areas of each region of the BLA were measured using ImageJ software (version 1.53; National Institutes of Health, Bethesda, MD, USA) and averaged within each mouse.

### 2.5. Electrophysiology

Under isoflurane anesthesia, the mice were transcardially perfused with ice-cold modified artificial cerebrospinal fluid (mACSF) containing 27 mM NaHCO<sub>3</sub>, 1.5 mM NaH<sub>2</sub>PO<sub>4</sub>, 2.5 mM KCl, 0.5 mM ascorbic acid, 1 mM CaCl<sub>2</sub>, 7 mM MgSO<sub>4</sub>, and 222.1 mM sucrose. The brain was rapidly removed and submerged in ice-cold oxygenated (95% O<sub>2</sub>/5% CO<sub>2</sub>) mACSF. Coronal brain blocks containing the basolateral amygdala were sliced at a thickness of 300 μm at a speed of 0.1 mm/s using a Leica



(caption on next page)

**Fig. 1.** Fluorescent reporter labeling of axo-axonic cells in the BLA. (A) Low-magnification confocal microscopy images of  $Vipr2^{+}$  cells (red) labeled with anti-NeuN (blue) and anti-PV (green) antibodies in the rostral to caudal part of the BLA. White arrows indicate  $PV^{+} Vipr2^{+}$  neurons. Scale bar, 100  $\mu m$ . (B) Triple fluorescence signals in the BLA of  $Vipr2$ -tdTomato mice generated by tdTomato (red), an anti-PV antibody (green), an anti-NeuN antibody (blue), and a merged image (merge). The white arrow indicates  $PV^{+} Vipr2^{+}$  neurons, and the yellow arrowhead indicates  $PV^{+} Vipr2^{-}$  neurons. Scale bar, 20  $\mu m$ . (C) Triple fluorescence signals in the BLA of  $Vipr2$ -tdTomato mice generated by tdTomato (red), an anti-GABA antibody (cyan), an anti-PV antibody (green), and a merged image (merge). The white arrow indicates  $PV^{+} Vipr2^{+}$  inhibitory neurons. Scale bar, 20  $\mu m$ . (D) High-magnification confocal microscopy images of the AIS labeled with an anti-ankyrin G antibody (green) and tdTomato<sup>+</sup> axon terminals (yellow arrows) labeled with an anti-PV antibody (blue) and an anti-VGAT antibody (white) in the BLA (upper). Yellow arrowheads indicate tdTomato<sup>+</sup> axo-axonic synapses (lower). Scale bar, 5  $\mu m$ . (E) Representative confocal microscopy image of  $NeuN^{+}Vipr2^{+}$  cells (white arrows) and  $NeuN^{+}Vipr2^{-}$  cells (yellow arrows) in the BLA. Scale bar, 20  $\mu m$ . (F) Representative confocal microscopy image of  $NeuN^{+}Vipr2^{-}$  cells (yellow arrowheads) labeled with an anti-GFAP antibody (left) and an anti-SOX10 antibody (center; green) and  $NeuN^{+}Vipr2^{+}$  cells (yellow arrowheads) labeled with an anti-CaMKII antibody (right). White arrows indicate  $CaMKII^{+}NeuN^{+}Vipr2^{-}$  cells. Scale bar, 20  $\mu m$ . (G) The average fraction of  $Vipr2^{+}$  neurons that are  $PV^{+}$  in the rostrocaudal axis of the LA (black) and BA (red). Error bars indicate the SEM.  $n = 7$  mice, Wilcoxon rank sum test,  $**P < 0.01$ . (H) The average density of  $Vipr2^{+}PV^{+}$  neurons in the rostrocaudal axis of the LA (black) and BA (red). Error bars indicate the SEM.  $n = 7$  mice, one-way ANOVA with Tukey's post hoc test,  $**P < 0.01$ . (I) The average fraction of  $PV^{+}$  neurons that are labeled with  $Vipr2$ -tdTomato in the rostrocaudal axis of the LA (black) and BA (red). (J) The average fraction of tdTomato<sup>+</sup> on AIS-contacting  $VGAT^{+}$  puncta in the BLA. Error bars indicate the SEM.  $n = 8$  mice.

vibratome (VT1200S, Leica Microsystems, Nussloch, Germany). The slices were left to recover at 35 °C for 30 min in oxygenated artificial cerebrospinal fluid (aCSF) containing 127 mM NaCl, 26 mM NaHCO<sub>3</sub>, 1.6 mM KCl, 1.24 mM KH<sub>2</sub>PO<sub>4</sub>, 1.3 mM MgSO<sub>4</sub>, 2.4 mM CaCl<sub>2</sub>, and 10 mM glucose. Experiments were performed in a submerged chamber perfused at 3–4 ml/min with oxygenated ACSF at 32 °C. Borosilicate glass pipettes (4–8 M $\Omega$ ) were filled with a potassium-based solution containing 120 mM potassium gluconate, 5 mM KCl, 10 mM HEPES, 10 mM disodium phosphocreatine, 2 mM Mg-ATP, 0.1 mM Na<sub>2</sub>-GTP, 0.2 mM EGTA and 0.2% biocytin. Slices were visualized using an upright microscope (ECLIPSE-FN1; Nikon) fitted with an infrared differential interference contrast, 40 $\times$  water immersion objective (CFI Apo NIR 40X W; Nikon), halogen lamp (LS-DWL-N; Sumita optical glass Inc., Saitama, Japan) and fluorescent lamp (C-LHG1; Nikon). Neurons were imaged with a CCD camera (C3077-78; Hamamatsu Photonics, Shizuoka, Japan). The signals were amplified and digitized at a sampling rate of 20 kHz using a MultiClamp 700B amplifier and a Digidata 1440A digitizer controlled by Clampex 10.7 software (Molecular Devices, San Jose, CA, USA). The liquid junction potentials were automatically corrected before each experiment using the Pipette Offset mode (Molecular Devices) and were not corrected post hoc. tdTomato-positive neurons were injected with a step current injection for 800 ms (−40 pA to 520 pA, 20–40 pA steps) to determine intrinsic action potential properties. After recording, the slices were fixed in 4% PFA/PB at 4 °C for 2–7 days. To visualize the recorded neurons, the slices were blocked with 5% BSA and 0.5% Triton X-100 in PBS for 1 h at room temperature, incubated for 2 nights at 4 °C with rabbit polyclonal anti-parvalbumin primary antibody (1:2000), and then incubated overnight at 4 °C with donkey anti-rabbit Alexa Fluor 488 and 1  $\mu g/ml$  streptavidin-conjugated Alexa Fluor 647 secondary antibodies. Labeled slices were mounted onto microscope slides with CC/Mount (K002; Diagnostic BioSystems Inc., Pleasanton,

CA, USA). The slices were scanned using a laser scanning confocal microscope (A1-HD25; Nikon) equipped with 10 $\times$ , 20 $\times$ , and 40 $\times$  air objectives.

## 2.6. Statistical analysis

The results are presented as the mean  $\pm$  SEM. Data were statistically compared with Student's t test, the Wilcoxon rank sum test, or one-way ANOVA followed by Tukey's post hoc test. No statistical methods were used to predetermine sample sizes, but the sample sizes used were similar to those reported in the field for similar experiments (Taniguchi et al., 2013; Kawaguchi and Kubota, 1998). The criterion for statistical significance was set at  $P < 0.05$ .

## 3. Results

To demonstrate whether AACs are selectively labeled in the basolateral amygdala (BLA) of  $Vipr2$ -IRES2-Cre mice, we prepared coronal slices containing the BLA from  $Vipr2$ -IRES2-Cre knock-in mice crossed with an *Ai14* reporter mouse.  $Vipr2$ -tdTomato cells were widespread in the rostral to caudal part of the BLA, and some of these cells were parvalbumin-positive ( $PV^{+}$ ) (Fig. 1A). These cells exhibited immunoreactivity to NeuN (Fig. 1B) and  $\gamma$ -aminobutyric acid (GABA, Fig. 1C). Importantly, tdTomato<sup>+</sup> GABAergic axon terminals made contacts with the axon initial segment (AIS) that was positive for ankyrin G (Fig. 1D), a reliable marker of the AIS of pyramidal neurons (Bienvenu et al., 2012; Veres et al., 2014). Furthermore, in  $Vipr2$ -tdTomato mice,  $97.13 \pm 0.78\%$  of AIS-contacting  $VGAT^{+}$  puncta (putative axo-axonic synapse) were tdTomato<sup>+</sup> ( $n = 1702$  AIS-contacting  $VGAT^{+}$  puncta from 8 mice, Fig. 1J). Although some tdTomato<sup>+</sup> cells presented glial cell-like morphology and exhibited immunoreactivity for GFAP and SOX10

**Table 1**  
Anatomical profiling of the  $Vipr2^{+}$  axon terminal and  $Vipr2^{+}$  cells.

| Reporter   | Axon-terminal type                              | $Vipr2^{+}PV^{+}$ (%)                       |   |
|--|---|---|---|
| $Vipr2$ -Cre/ <i>Ai14</i> (Fig. 1)                   | AIS-contacting $VGAT^{+}$ puncta<br>(n =)       | 69.18 $\pm$ 2.77                            | (961 puncta from 4 mice)                    |
| $Vipr2$ -Cre/AAV-FLEX-Synaptophysin-mCherry (Fig. 3) |   | 80.68 $\pm$ 8.93                            | (485 puncta from 2 mice)                    |
| Reporter   | Cell type                                       | GABA <sup>+</sup> (%)                       | CaMKII <sup>+</sup> (%)                     |
| $Vipr2$ -Cre/ <i>Ai14</i> (Fig. 1)                   | $Vipr2$ -tdTomato <sup>+</sup> neurons<br>(n =) | 87.65 $\pm$ 2.88<br>(180 cells from 4 mice) | 14.38 $\pm$ 2.85<br>(111 cells from 4 mice) |
| $Vipr2$ -Cre/AAV-FLEX-GFP (Fig. 3)                   | $Vipr2$ -GFP <sup>+</sup> cells<br>(n =)        | 94.34 $\pm$ 0.10<br>(317 cells from 6 mice) | N.T.  |

Data are given as the mean  $\pm$  SEM. (N.T.: not tested). (Fig. 1, Fig. 3, Fig. 1 and Fig. 3).

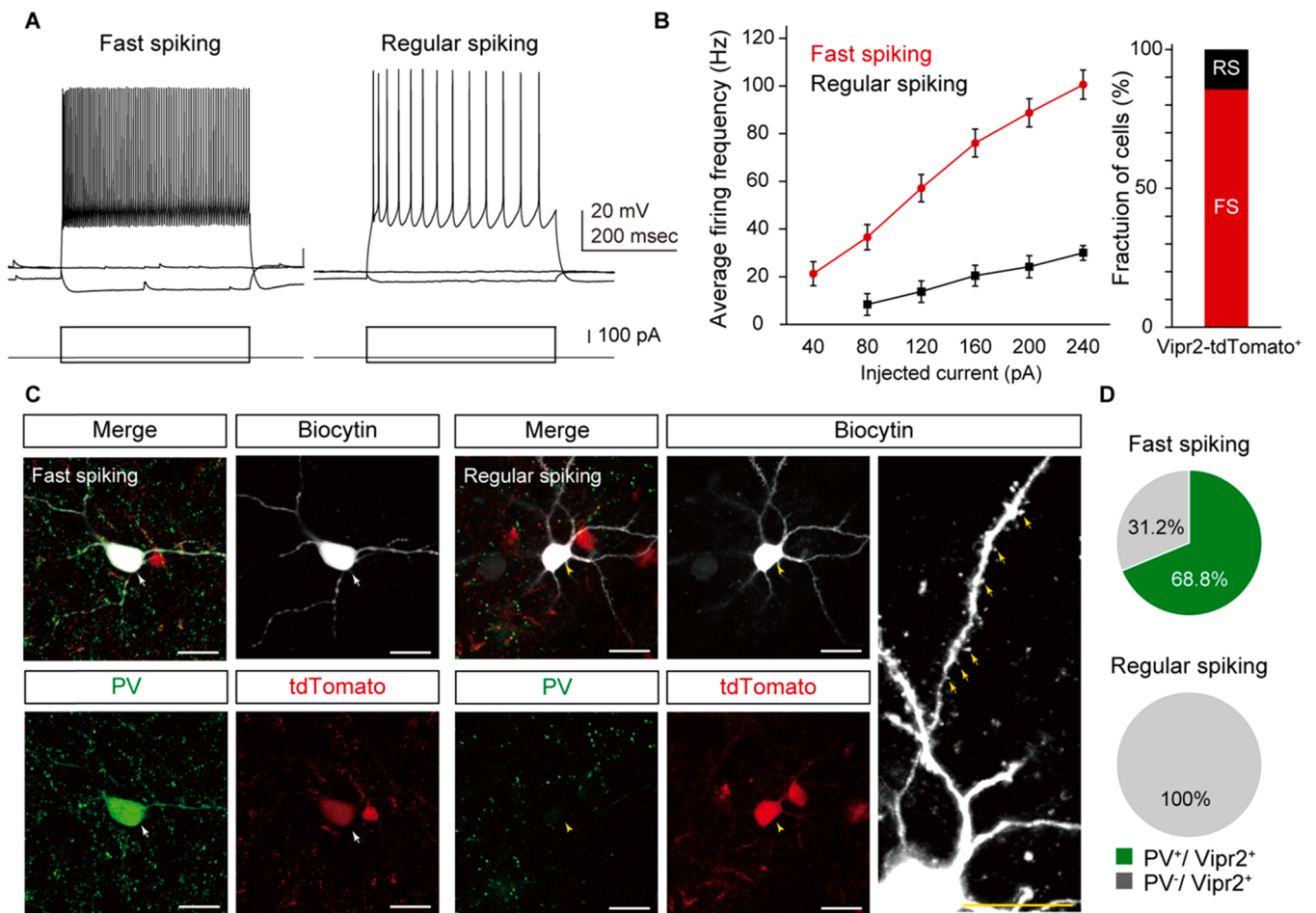


**Fig. 2.** Electrophysiological recordings of Vipr2<sup>+</sup> neurons. (A) Whole-cell current clamp recording from fast-spiking and regular-spiking Vipr2<sup>+</sup> neurons in the BLA. (B) Stimulus–response curves for Vipr2<sup>+</sup> neurons based on the electrophysiological profile (fast spiking: n = 18 cells, regular spiking: n = 3 cells). (C) Biocytin-filled Vipr2-tdTomato<sup>+</sup> fast-spiking neurons (left) and regular-spiking neurons (right) labeled with an anti-PV antibody (green). Yellow arrows indicate dendritic spines of Vipr2-tdTomato<sup>+</sup> regular-spiking neurons. Scale bar, 20  $\mu$ m. (D) Fraction of PV<sup>+</sup> fast-spiking and regular-spiking neurons.

(Fig. 1E, F), approximately 50% of NeuN<sup>+</sup>Vipr2<sup>+</sup> cells in the BLA were also PV<sup>+</sup>. Moreover,  $87.65 \pm 2.88\%$  and  $14.38 \pm 2.85\%$  of NeuN<sup>+</sup>tdTomato<sup>+</sup> cells were GABAergic (GABA<sup>+</sup>) and excitatory neurons (CaMKII<sup>+</sup>, a marker for pyramidal neurons in the BLA, Morikawa et al., 2017) (Fig. 1F, Table 1), respectively.  $61.1 \pm 8.17\%$  of PVNeuN<sup>+</sup>tdTomato<sup>+</sup> neurons were GABAergic neurons. These results suggest that approximately 20–30% of Vipr2<sup>+</sup> cells are PV<sup>+</sup> GABAergic cells. The fraction of PV<sup>+</sup> neurons was higher in the basal amygdala (BA) than in the lateral amygdala (LA) (total LA:  $38.6 \pm 3.9\%$ ; total BA:  $53.8 \pm 2.25\%$ , n = 1438 tdTomato<sup>+</sup> cells from 172 slices of 7 mice; Wilcoxon rank sum test,  $W = 31$ ,  $P = 0.0041$ ; Fig. 1G). Furthermore, Vipr2<sup>+</sup>PV<sup>+</sup> neurons were more abundant in the caudal part of the BA than in the rostral region of the LA and BA (caudal BA:  $15.08 \pm 2.06$  cells/mm<sup>2</sup>; one-way ANOVA,  $F_{5, 36} = 3.89$ ,  $P = 0.008$  vs. rostral LA:  $6.00 \pm 2.08$  cells/mm<sup>2</sup>,  $P = 0.0086$  vs. rostral BA:  $6.08 \pm 1.76$  cells/mm<sup>2</sup>,  $P = 0.0096$ ; LA:  $7.86 \pm 0.58$  cells/mm<sup>2</sup>, BA:  $10.84 \pm 0.51$  cells/mm<sup>2</sup>,  $t$  test,  $t_6 = 3.89$ ,  $P = 0.0081$ , n = 1438 tdTomato<sup>+</sup> cells from 172 slices of 7 mice; Fig. 1H), and ~20% of PV<sup>+</sup> cells in the BLA were tdTomato<sup>+</sup> (rostral LA:  $22.69 \pm 7.29\%$ , medial LA:  $20.14 \pm 2.56\%$ , caudal LA:  $17.66 \pm 3.70\%$ , rostral BA:  $12.57 \pm 2.46\%$ , medial BA:  $15.54 \pm 1.91\%$ , caudal BA:  $18.61 \pm 2.07\%$ , n = 4312 PV<sup>+</sup> cells from 172 slices of 7 mice; Fig. 1I). These results suggest that Vipr2 is an appropriate genetic marker of AACs in the BLA.

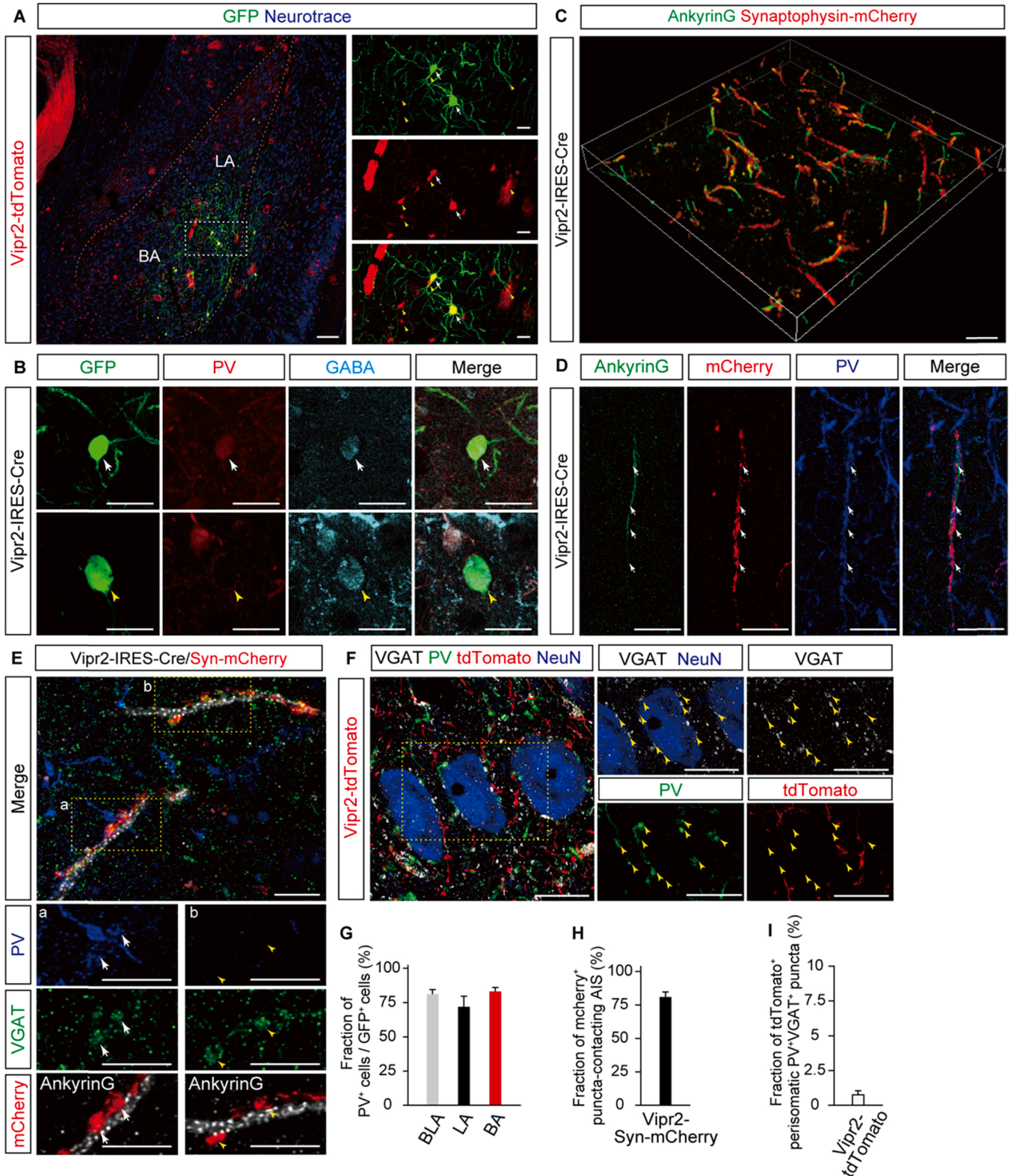
Next, we conducted patch clamp recordings to characterize the electrophysiological properties of Vipr2<sup>+</sup> neurons in the BLA. We prepared acute brain slices from Vipr2-tdTomato mice. Upon intracellular

current injection, 18 out of 21 Vipr2<sup>+</sup> neurons showed fast spiking, and 3 out of 21 cells showed regular spiking (n = 21 cells from 5 mice; Fig. 2A, B, C). The majority of Vipr2<sup>+</sup> fast-spiking neurons were immunolabeled with PV and exhibited spine-sparse dendrites (Fig. 2C, D), a feature of traditionally defined AACs (Vereczki et al., 2016), while PV-negative Vipr2<sup>+</sup> regular spiking neurons exhibited the morphology of pyramidal neurons, which have dendritic spines (Ryan et al., 2016). These results indicate that most Vipr2<sup>+</sup> neurons show electrophysiological and morphological characteristics similar to those of AACs in the BLA.

Transgenic strategies often lead to labeling of both AACs and other cell types, such as glial cells and pyramidal neurons (Figs. 1 and 2), likely due to off-target Cre recombinase expression during development. To avoid this problem, we used the FLEX-switch target system (Atasoy et al., 2008). We injected adeno-associated virus (AAV) containing Cre-dependent GFP or synaptophysin-mCherry into the BLA of Vipr2-tdTomato mice or Vipr2-IRES2-Cre mice. We found that the majority of GFP-labeled cells were immunoreactive for PV and GABA (Fig. 3A, B, C), and axon terminals labeled with synaptophysin-mCherry frequently contacted the AIS in the BLA (Fig. 3D, E, H).  $94.34 \pm 0.10\%$  of Vipr2<sup>+</sup> neurons exhibited immunoreactivity for GABA (Fig. 3B, Table 1). Notably, approximately 20–30% of VGAT<sup>+</sup>Vipr2<sup>+</sup> puncta on AISs were PV<sup>+</sup> (Fig. 3E, Table 1). Consistently, approximately 20% of GFP<sup>+</sup> cells were not immunolabeled for PV (Fig. 3B, G). Importantly, we did not find GFP<sup>+</sup> signals in glial cells (Fig. 3A). Approximately 80% of GFP<sup>+</sup> cells were PV<sup>+</sup> (BLA:  $81.2 \pm 3.3\%$ , LA:  $71.9 \pm 7.8\%$ , BA:  $83.2$

$\pm 2.9\%$ ,  $n = 1042$  GFP<sup>+</sup> cells from 150 slices of 5 mice; Fig. 3C) and locally innervated the AIS of pyramidal neurons (Fig. 3A). Consistent with Fig. 1J,  $80.9 \pm 3.77\%$  of Vipr2-synaptophysin-mCherry<sup>+</sup> puncta were associated with the AIS ( $n = 841$  AISs from 3 mice, Fig. 3H). Moreover, most axon terminals from PV<sup>+</sup> basket cells in the BLA of

Vipr2-tdTomato mice were not labeled with tdTomato, and Vipr2<sup>+</sup> puncta were rarely observed around the cell bodies ( $n = 933$  VGAT<sup>+</sup> puncta from 4 mice, Fig. 3F, I). These results indicate that most AIS of BLA neurons are innervated by Vipr2-AACs and that PV<sup>+</sup> cells expressing Vipr2 are anatomically distinct from basket cells.



(caption on next page)

**Fig. 3.** AAC-specific labeling in the BLA using AAV. (A) Low-magnification (left) and high-magnification (right) confocal microscopy images of *Vipr2*<sup>+</sup> cells labeled with GFP in the BLA of *Vipr2*-tdTomato mice. White arrows indicate *Vipr2*<sup>+</sup>GFP<sup>+</sup> cells, and yellow arrows indicate *Vipr2*<sup>+</sup> glial cells that do not express GFP. Scale bar, 20  $\mu$ m. (B) Representative confocal microscopy images of triple fluorescence signals in the BLA of *Vipr2*-Cre mice generated by GFP (green), an anti-PV antibody (red), an anti-GABA antibody (cyan), and a merged image (merge). White arrows and yellow arrowheads indicate *Vipr2*-GFP<sup>+</sup>PV<sup>+</sup> inhibitory neurons (upper) and PV inhibitory neurons (bottom), respectively. Scale bar, 20  $\mu$ m. (C) 3D image created from confocal microscopy images of the AIS labeled with an anti-ankyrin G antibody (green) and synaptophysin-mCherry (red)-labeled axon terminals in the BLA. Scale bar, 10  $\mu$ m. (D) High-magnification confocal microscopy images of the AIS contact site (white arrows) of synaptophysin-mCherry<sup>+</sup> (mCherry, red) axon terminals labeled with an anti-PV antibody (blue). Scale bar, 10  $\mu$ m. (E) Representative confocal microscopy images of triple fluorescence staining in the BLA of *Vipr2*-synaptophysin-mCherry (Syn-mCherry) mice generated by mCherry (red), an anti-VGAT antibody (green), an anti-PV antibody (blue), an anti-ankyrin G antibody (white), and a merged image (upper). White arrows indicate PV<sup>+</sup> *Vipr2*<sup>+</sup> axo-axonic synapses (a) and PV *Vipr2*<sup>+</sup> axo-axonic synapses. Scale bar, 5  $\mu$ m. (F) Representative confocal microscopy images of triple fluorescence staining in the BLA of *Vipr2*-tdTomato mice generated by tdTomato (red), an anti-VGAT antibody (white), an anti-NeuN antibody (blue), an anti-PV antibody (green), and a merged image (left). Yellow arrowheads indicate VGAT<sup>+</sup> axon terminals containing PV from basket cells. Scale bar, 10  $\mu$ m. (G) The average fraction of *Vipr2*-GFP<sup>+</sup> neurons that are PV<sup>+</sup> in the rostrocaudal axis of the BLA (gray), LA (black) and BA (red). Error bars indicate the SEM. n = 5 mice. (H) The average fraction of mCherry<sup>+</sup> puncta-contacting AIS in the BLA of *Vipr2*-synaptophysin-mCherry (Syn-mCherry) mice. Error bars indicate the SEM. n = 3 mice. (I) The average fraction of *Vipr2*-tdTomato<sup>+</sup> (tdTomato<sup>+</sup>) perisomatic PV<sup>+</sup>VGAT<sup>+</sup> puncta in the BLA of *Vipr2*-tdTomato mice. Error bars indicate the SEM. n = 4 mice.

#### 4. Discussion

In this study, we characterized AACs in the BLA based on *Vipr2* expression. Most *Vipr2*<sup>+</sup> neurons exhibited the anatomical and electrophysiological properties of traditionally defined AACs in the BLA. Although some *Vipr2*<sup>+</sup> neurons showed no immunolabeling for PV, the first marker of AACs, these results are consistent with the findings of a previous report that approximately 30% of AACs lack immunoreactivity for PV (Vereczki et al., 2021). Importantly, almost all axo-axonic synapses were *Vipr2*<sup>+</sup> but not at the cell body (Figs. 1J and 3I). Furthermore, approximately 80% of *Vipr2*-syn-mCherry<sup>+</sup> puncta were associated with the AIS in the BLA (Fig. 3H). These results indicate that *Vipr2* is a suitable genetic marker of AACs in the BLA and that AACs can be selectively labeled at the adult stage in *Vipr2*-IRES2-Cre mice using AAV expression.

An early study reported that the fate-mapping strategy using *Nkx2.1*-CreER mice captures chandelier cell progenitors in the cortex (Taniguchi et al., 2013); however, it is necessary to validate whether this strategy is still effective in the BLA. Remarkably, approximately 50% and 85% of *Nkx2.1* cells are PV-negative in the sensory cortex and medial prefrontal cortex, respectively, although these cells exhibit a chandelier-like shape and the classical morphology of AACs in the cortex (He et al., 2016; Taniguchi et al., 2013). Unlike those in the cortex, AACs in the BLA do not display a chandelier-like morphology (Veres et al., 2014); therefore, the analysis of AACs based on PV expression, a traditionally defined marker for AACs, must be further validated, and we may have underestimated the fraction of AACs in the *Vipr2*<sup>+</sup> cell group. In the patch clamp recording experiments, the fraction of PV-positive fast-spiking *Vipr2*<sup>+</sup> neurons was 68.8% (Fig. 2D). Fast-spiking properties are dependent on *Kv3* subfamily expression (Massengill et al., 1997; Martina et al., 1998), and some *Kv3* cells do not express PV (Chow et al., 1999). This difference in PV content levels among fast-spiking neurons might reflect variations in physiological states (Taniguchi et al., 2013; Donato et al., 2013). Furthermore, some *Vipr2*<sup>+</sup> neurons exhibited pyramidal neuron-like morphology and electrophysiological properties but were not labeled with PV (Fig. 2); however, we cannot exclude the possibility that these neurons are excitatory AACs, as asymmetric synapses are formed at the AIS of thalamic reticular neurons (Pinaut et al., 1997). To address these questions, the most effective approach is to target intersectional populations of neuron subtypes (Fenno et al., 2014) or to utilize AAV-containing promoters and enhancers to access specific cell types, such as the *CaMK2* promoter for excitatory neurons in combination with immunostaining for *Vglut1* or *Vglut2* (O'Leary et al., 2020; Nakamura et al., 2007) and the *mDlx* enhancer for inhibitory neuron targeting (Dimidschstein et al., 2016).

Although conventional research on AACs in the BLA has been dependent on anatomical techniques, we propose that a combination of genetic approaches is a powerful tool for the selective modulation of the brain region-specific activity of AACs to elucidate the mechanisms of emotional processing in the amygdala.

#### Author contributions

S.M. and Y.I. designed the research; M.N. and S.M. performed the histological experiments; S.M. performed the patch clamp recordings; M.N. and S.M. contributed to the figures and analyzed data; and S.M. and Y.I. wrote the manuscript. All authors discussed the manuscript and approved the final version.

#### Acknowledgments

This work was supported by JST ERATO (JPMJER1801 to Y.I.), the Institute for AI and Beyond of the University of Tokyo, and JSPS Grants-in-Aid for Scientific Research (18H05525 to Y.I., 20K15925 to S.M.). We are grateful to Dr. Haruki Takeuchi for valuable comments.

#### References

- Atasoy, D., Aponte, Y., Su, H.H., Sternson, S.M., 2008. A FLEX switch targets Channelrhodopsin-2 to multiple cell types for imaging and long-range circuit mapping. *J. Neurosci.* 28, 7025–7030. <https://doi.org/10.1523/JNEUROSCI.1954-08.2008>.
- Aurnhammer, C., Haase, M., Muether, N., Hausl, M., Rauschhuber, C., Huber, I., Nitschko, H., Busch, U., Sing, A., Ehrhardt, A., Baiker, A., 2012. Universal Real-Time PCR for the Detection and Quantification of Adeno-Associated Virus Serotype 2-Derived Inverted Terminal Repeat Sequences. *HUMAN GENE THERAPY METHODS* 23 (1), 18–28. <https://doi.org/10.1089/hgtb.2011.034>.
- Bienvenu, T.C.M., Busti, D., Magill, P.J., Ferraguti, F., Capogna, M., 2012. Cell-type-specific recruitment of amygdala interneurons to hippocampal theta rhythm and noxious stimuli in vivo. *Neuron* 74, 1059–1074. <https://doi.org/10.1016/j.neuron.2012.04.022>.
- Buhl, E.H., Halasy, K., Somogyi, P., 1994. Diverse sources of hippocampal unitary inhibitory postsynaptic potentials and the number of synaptic release sites. *Nature* 368, 823–828. <https://doi.org/10.1038/368823a0>.
- Chow, A., Erisir, A., Farb, C., Nadal, M.S., Ozaita, A., Lau, D., Welker, E., Rudy, B., 1999. *K $\chi$*  Channel Expression Distinguishes Subpopulations of Parvalbumin- and Somatostatin-Containing Neocortical Interneurons 19, 932–9345.
- DeFelipe, J., Hendry, S.H., Jones, E.G., 1989. Visualization of chandelier cell axons by parvalbumin immunoreactivity in monkey cerebral cortex. *Proc. Natl. Acad. Sci. USA* 86, 2093–7. doi: 10.1073/pnas.86.6.2093.
- Dimidschstein, J., Chen, Q., Tremblay, R., Rogers, S.L., Saldi, G.-A., Guo, L., Xu, Q., Liu, R., Lu, C., Chu, J., Grimley, J.S., Krostag, A.-R., Kaykas, A., Avery, M.C., Rashid, M.S., Baek, M., Jacob, A.L., Smith, G.B., Wilson, D.E., Kosche, G., Kruglikov, I., Rusielewicz, T., Kotak, V.C., Mowery, T.M., Anderson, S.A., Callaway, E.M., Dasen, J.S., Fitzpatrick, D., Fossati, V., Long, M.A., Noggle, S., Reynolds, J.H., Sanes, D.H., Rudy, B., Feng, G., Fishell, G., 2016. A viral strategy for targeting and manipulating interneurons across vertebrate species. *Nat. Neurosci.* 19, 1743–1749. <https://doi.org/10.1038/nn.4430>.
- Donato, F., Rompani, S.B., Caroni, P., 2013. Parvalbumin-expressing basket-cell network plasticity induced by experience regulates adult learning. *Nature* 504, 272–276. <https://doi.org/10.1038/nature12866>.
- Dudok, B., Szoboszlai, M., Paul, A., Klein, P., Liao, Z., Hwaun, E., Szabo, G., Geiller, T., Vancura, B., Wang, B., McKenzie, S., Homidan, J., Klaver, L.M., English, D., Huang, Z., Buzsáki, G., Losonczy, A., Soltesz, I., 2021. Recruitment and inhibitory action of hippocampal axo-axonic cells during behavior. *Neuron* 1–13. <https://doi.org/10.1016/j.neuron.2021.09.033>.
- Ego-Stengel, V., Wilson, M.A., 2010. Disruption of ripple-associated hippocampal activity during rest impairs spatial learning in the rat. *Hippocampus* 20, 1–10. <https://doi.org/10.1002/hipo.20707>.
- Fenno, L.E., Mattis, J., Ramakrishnan, C., Hyun, M., Lee, S.Y., He, M., Tucciarone, J., Selimbeyoglu, A., Berndt, A., Grosenick, L., Zalocusky, K.A., Bernstein, H., Swanson, H., Perry, C., Diester, I., Boyce, F.M., Bass, C.E., Neve, R., Huang, Z.J.,

- Deisseroth, K., 2014. Targeting cells with single vectors using multiple-feature Boolean logic. *Nat. Methods* 11, 763–772. <https://doi.org/10.1038/nmeth.2996>.
- Franklin, K.B.J., Paxinos, G., 2008. *The mouse brain in stereotaxic coordinates*, (3rd ed.). Academic Press.
- Girardeau, G., Benchenane, K., Wiener, S.I., Buzsáki, G., Zugaro, M.B., 2009. Selective suppression of hippocampal ripples impairs spatial memory. *Nat. Neurosci.* 12, 1222–1223. <https://doi.org/10.1038/nn.2384>.
- He, M., Tucciarone, J., Lee, S.H., Nigro, M.J., Kim, Y., Levine, J.M., Kelly, S.M., Krugikov, I., Wu, P., Chen, Y., Gong, L., Hou, Y., Osten, P., Rudy, B., Huang, Z.J., 2016. Strategies and tools for combinatorial targeting of GABAergic neurons in mouse cerebral cortex. *Neuron* 91, 1228–1243. <https://doi.org/10.1016/j.neuron.2016.08.021>.
- Kawaguchi, Y., Kubota, Y., 1998. Neurochemical features and synaptic connections of large physiologically-identified GABAergic cells in the rat frontal cortex. *Neuroscience* 85, 677–701. [https://doi.org/10.1016/S0306-4522\(97\)00685-4](https://doi.org/10.1016/S0306-4522(97)00685-4).
- Klausberger, T., Magill, P.J., Márton, L.F., Roberts, J.D.B., Cobden, P.M., Buzsáki, G., Somogyi, P., 2003. Brain-state- and cell-type-specific firing of hippocampal interneurons in vivo. *Nature* 421, 844–848. <https://doi.org/10.1038/nature01374>.
- LeDoux, J.E., 2000. Emotion circuits in the brain. *Annu. Rev. Neurosci.* 23, 155–184. <https://doi.org/10.1146/annurev.neuro.23.1.155>.
- Martina, M., Schultz, J.H., Ehmke, H., Monyer, H., Jonas, P., 1998. Functional and molecular differences between voltage-gated K<sup>+</sup> channels of fast-spiking interneurons and pyramidal neurons of rat hippocampus. *J. Neurosci.* 18, 8111–8125. <https://doi.org/10.1523/jneurosci.18-20-08111.1998>.
- Massengill, J.L., Smith, M.A., Son, D.I., Dowd, D.K.O., 1997. Massengill ODowd 97JNS Kv3.1 develop in cortical neurons.pdf. *Differ. Expr. K4-AP Curr. sand Kv3.1 potassium channel Transcr. cortical neurons that Dev. distinct firing phenotypesexpression K4-AP Curr. sand Kv3.1 potassium channel Transcr. cortical neurons t 17*, 3136–3147.
- Morikawa, S., Ikegaya, Y., Narita, M., Tamura, H., 2017. Activation of perineuronal net-expressing excitatory neurons during associative memory encoding and retrieval. *Sci. Rep.* 7, 46024. <https://doi.org/10.1038/srep46024>.
- Nakamura, K., Watakabe, A., Hioki, H., Fujiyama, F., Tanaka, Y., Yamamori, T., Kaneko, T., 2007. Transiently increased colocalization of vesicular glutamate transporters 1 and 2 at single axon terminals during postnatal development of mouse neocortex: a quantitative analysis with correlation coefficient. *Eur. J. Neurosci.* 26, 3054–3067. <https://doi.org/10.1111/j.1460-9568.2007.05868.x>.
- O’Leary, T.P., Sullivan, K.E., Wang, L., Clements, J., Lemire, A.L., Cembrowski, M.S., 2020. Extensive and spatially variable within-cell-type heterogeneity across the basolateral amygdala. *Elife* 9, e59003. <https://doi.org/10.7554/eLife.59003>.
- Perumal, M.B., Latimer, B., Xu, L., Stratton, P., Nair, S., Sah, P., 2021. Microcircuit mechanisms for the generation of sharp-wave ripples in the basolateral amygdala: a role for chandelier interneurons. *Cell Rep.* 35 <https://doi.org/10.1016/j.celrep.2021.109106>.
- Peters, A., Proskauer, C.C., Ribak, C.E., 1982. Chandelier cells in rat visual cortex. *J. Comp. Neurol.* 206, 397–416. <https://doi.org/10.1002/cne.902060408>.
- Pinault, D., Smith, Y., Deschênes, M., 1997. Dendrodendritic and axoaxonic synapses in the thalamic reticular nucleus of the adult rat. *J. Neurosci.* 17, 3215–3233. <https://doi.org/10.1523/jneurosci.17-09-03215.1997>.
- Price, J., 1987. part I: Hypothalamus, hippocampus, amygdala, retina. In *The limbic region. I: The amygdaloid complex. Handbook of Chemical Neuroanatomy/Vol. 5, Integrated systems of the CNS*. Elsevier, pp. 279–389.
- Ryan, S.J., Ehrlich, D.E., Rainnie, D.G., 2016. Morphology and dendritic maturation of developing principal neurons in the rat basolateral amygdala. *Brain Struct. Funct.* 221, 839–854. <https://doi.org/10.1007/s00429-014-0939-x>.
- Sah, P., Faber, E.S.L., De Armentia, M.L., Power, J., 2003. The amygdaloid complex: anatomy and physiology. *Physiol. Rev.* 83, 803–834. <https://doi.org/10.1152/physrev.00002.2003>.
- Schneider-Mizell, C.M., Bodor, A.L., Collman, F., Brittain, D., Bleckert, A., Dorkenwald, S., Turner, N.L., Macrina, T., Lee, K., Lu, R., Wu, J., Zhuang, J., Nandi, A., Hu, B., Buchanan, J., Takeno, M.M., Torres, R., Mahalingam, G., Bumbarger, D.J., Li, Y., Chartrand, T., Kemnitz, N., Silversmith, W.M., Ih, D., Zung, J., Zlateski, A., Tartavull, I., Popovych, S., Wong, W., Castro, M., Jordan, C.S., Froudarakis, E., Becker, L., Suckow, S., Reimer, J., Tolias, A.S., Anastassiou, C.A., Seung, H.S., Reid, R.C., Costa, N.M. da, 2021. Structure and function of axo-axonic inhibition. *Elife* 10, 1–39. <https://doi.org/10.7554/eLife.73783>.
- Somogyi, P., 1977. A specific ‘axo-axonal’ interneuron in the visual cortex of the rat. *Brain Res.* 136, 345–350. [https://doi.org/10.1016/0006-8993\(77\)90808-3](https://doi.org/10.1016/0006-8993(77)90808-3).
- Somogyi, P., Freund, T.F., Hodgson, A.J., Somogyi, J., Beroukas, D., Chubb, I.W., 1985. Identified axo-axonic cells are immunoreactive for GABA in the hippocampus visual cortex of the cat. *Brain Res.* 332, 143–149. [https://doi.org/10.1016/0006-8993\(85\)90397-X](https://doi.org/10.1016/0006-8993(85)90397-X).
- Taniguchi, H., Lu, J., Huang, Z.J., 2013. The spatial and temporal origin of chandelier cells in mouse neocortex. *Science* 339 (80), 70–74. <https://doi.org/10.1126/science.1228246>.
- Tasic, B., Yao, Z., Graybiel, L.T., Smith, K.A., Nguyen, T.N., Bertagnolli, D., Goldy, J., Garren, E., Economo, M.N., Viswanathan, S., Penn, O., Bakken, T., Menon, V., Miller, J., Fong, O., Hirokawa, K.E., Lathia, K., Rimorin, C., Tieu, M., Larsen, R., Casper, T., Barkan, E., Kroll, M., Parry, S., Shapovalova, N.V., Hirschstein, D., Pendergraft, J., Sullivan, H.A., Kim, T.K., Szafer, A., Dee, N., Groblewski, P., Wickersham, I., Cetin, A., Harris, J.A., Levi, B.P., Sunkin, S.M., Madisen, L., Daigle, T.L., Looger, L., Bernard, A., Phillips, J., Lein, E., Hawrylycz, M., Svoboda, K., Jones, A.R., Koch, C., Zeng, H., 2018. Shared and distinct transcriptomic cell types across neocortical areas. *Nature* 563, 72–78. <https://doi.org/10.1038/s41586-018-0654-5>.
- Vereczki, V.K., Müller, K., Krizsán, É., Máté, Z., Fekete, Z., Rovira-Esteban, L., Veres, J.M., Erdélyi, F., Hájos, N., 2021. Total number and ratio of GABAergic neuron types in the mouse lateral and basal amygdala. *J. Neurosci.* 41, 4575–4595. <https://doi.org/10.1523/JNEUROSCI.2700-20.2021>.
- Vereczki, V.K., Veres, J.M., Müller, K., Nagy, G.A., Rác, B., Barsy, B., Hájos, N., 2016. Synaptic organization of perisomatic gabaergic inputs onto the principal cells of the mouse basolateral amygdala. *Front. Neuroanat.* 10 <https://doi.org/10.3389/fnana.2016.00020>.
- Veres, J.M., Nagy, G.A., Vereczki, V.K., András, T., Hájos, N., 2014. Strategically positioned inhibitory synapses of axo-axonic cells potentially control principal neuron spiking in the basolateral amygdala. *J. Neurosci.* 34, 16194–16206. <https://doi.org/10.1523/JNEUROSCI.2232-14.2014>.